ACS APPLIED MATERIALS & INTERFACES

Research Article

www.acsami.org

Liquid-Phase Pulsed Laser Ablation and Electrophoretic Deposition for Chalcopyrite Thin-Film Solar Cell Application

Wei Guo* and Bing Liu

IMRA America Inc., 1044 Woodridge Avenue, Ann Arbor, Michigan 48105

Supporting Information

ABSTRACT: We report ligand-free synthesis of colloidal metallic nanoparticles using liquid-phase pulsed laser ablation, and electrophoretic deposition of the nanoparticles for fabrication of $Cu(In,Ga)Se_2$ (CIGS) thin film solar cells. First, colloidal metallic nanoparticles of Cu−In and Cu−Ga alloys are produced by pulsed laser ablation in common organic solvents without using stabilizing ligands. The nanoparticles are examined for phase, composition, and electrical surface charging and charge modulation mechanisms. Metallic precursor thin films with high purity and precise composition are produced by electrophoretic deposition of the colloids without transferring to another solvent and without using binders. Finally, we demonstrate fabrication of CIGS solar cells on Mo sheet substrates with an (active area) energy conversion efficiency up to 7.37%.

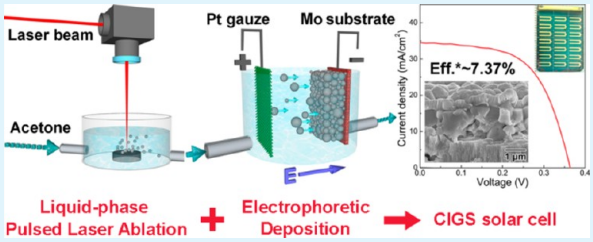

KEYWORDS: *metallic nanoparticle, ligand-free, surface charge, electrophoretic deposition, pulsed laser ablation, CIGS, solar cell*

1. INTRODUCTION

Chalcopyrite materials $CuInSe_2$ (CIS), $Cu(In,Ga)Se_2$ (CIGS), and $Cu_2ZnSn(S,Se)_4$ (CZTS) are considered promising solar absorber materials for their high adsorption coefficients and high internal quantum efficiencies.[1] The record conversion efficiency has reached 20.3% for CIGS thin film solar cells deposited using vacuum co-evaporation.[2,3] To reduce the production cost, non-vacuum solution-based fabrication methods have been developed, and lab-scale cell efficiencies have reached 15.2% for CIGS and 11.1% for CZTS using hydrazine as the solvent.[4,5] Other solution-based approaches using less toxic solvents include electrodeposition[6−9] and coating of metal salt[10−12] or organometallic[13] precursor solutions by mechanical processes such as spraying or spin coating.

A promising alternative route to fabricate chalcopyrite thin film solar cell is to use particles as precursors in the form of ink or colloid. There have been several colloid methods for synthesizing quaternary and ternary chalcogenide nanocrystals,[14−20] and efficiency up to 12.0% has been reported.[20] Oxide[21] and metallic alloy[22] large particles (micrometer-size powders) produced by mechanical breakdown have also been used in fabricating 13.6%-efficient CIGS solar cells.[21] Compared with quaternary and ternary particles, metallic alloy particles have the potential to lead to higher cell efficiency, because they have relatively low melting temperatures which promote film densification during selenization. Indeed, when using oxide particles as precursors, an additional hydrogen reduction process is required to convert oxide to metal before selenization.[21] The use of small metallic particles on the nanoscale in fabricating chalcopyrite solar absorber is first carried out by Kaelin et al.,[23] showing dense CIGS films but no cell efficiency because of the existence of In_2O_3 impurity phase. To the best of our knowledge, the only chalcopyrite solar cell fabricated from metallic nanoparticles is reported by Chen et al.[24] with efficiency up to 1.48%, limited by residual impurities of chemical reactants and stabilizers.

Residual organic impurity in the particle synthesis process is the main obstacle for the application of metallic-nanoparticle-based approach. Colloidal metallic nanoparticles are usually synthesized by chemical reduction of metal salts or decomposition of organometallic compounds in appropriate solvents.[25] In order to stabilize the particles from aggregation due to the van der Waals attraction, the particle surfaces are either electrostatically charged with organic ligands or sterically stabilized with polymer coatings.[25,26] Additional ligand exchange steps are needed to transfer the particles into the target solvent for final applications. The stabilizers (ligands and polymers) are often considered impurities, and extensive research is on-going to either minimize their content or replace with smaller inorganic anions.[27] Besides the stabilizers, another significant source of impurities in particle-based methods comes from the organic binders used for increasing the colloid viscosity during precursor film coating.

In this paper, we report a new metallic-nanoparticle-based approach for fabricating thin film CIGS solar cells, comprising (1) liquid-phase femtosecond pulsed laser ablation for producing metallic nanoparticle colloids, (2) electrophoretic deposition of the nanoparticle colloids into precursor thin films, and (3) selenization of the precursor films. In particular, this

Received: October 11, 2012
Accepted: December 3, 2012
Published: December 3, 2012

   dx.doi.org/10.1021/am3022976 | ACS Appl. Mater. Interfaces 2012, 4, 7036−7042

approach only uses common organic solvents such as ketones or alcohols, and does not require any stabilizing ligands and binders, hence significantly improving the film purity and reducing the health hazards during fabrication.

Liquid-phase pulsed laser ablation (LP-PLA) is a recently developed method for synthesizing nanoparticle colloids.[28,29] In this method, a pulsed laser beam is focused on a target that is submerged in a liquid solvent, and laser ablation, particle formation, and particle dispersion occur simultaneously in the solvent. The advantages of LP-PLA include a wide range of applicable materials and many choices of solvents. Moreover, due to the laser-plasma-induced surface charge that can automatically stabilize the nanoparticles against aggregation, no stabilizing ligands are required, assuring very high colloid purity. The main drawbacks include a relatively broad particle size distribution and relatively low production rate. In this work, we employ an ultrashort femtosecond laser with a MHz-range high repetition rate to produce metallic nanoparticles with narrower size distribution and higher throughput.

Electrophoretic deposition (EPD) is a thin film deposition method based on the electrokinetic mobility of colloidal particles acquired under an external electric field. The method is traditionally used in automotive and appliance industries for coating thick films of micrometer-size particles on a substrate, which serves as one of the electrodes used for applying the electric field.[30] Recently, there has been an increasing interest in its application in depositing nanoparticles.[31] EPD offers a significant advantage of film densification induced by strong electrical force near the electrode (substrate) surface, therefore eliminating the reliance on adhesives and binders. It is also applicable to deposition on flexible substrates and on substrates with complex surface shapes. However, in order to deposit a smooth and crack-free thin film, many factors need to be carefully considered, including particle surface charge, electrical and fluidic properties of solvents, choice of electrode material, and current-voltage characteristics. Particularly in this work, cathodic EPD, where the substrate works as the cathode, is preferred to avoid potential oxidation of the metallic nanoparticles and substrate that can occur on the anode side. This requires control of the nanoparticle surface charge, which is effectively realized by introducing low concentration of trivalent cations of In or Ga into the colloid.

In the following of this paper, we first present details of LP-PLA, EPD, selenization, and solar cell fabrication in the Experimental Methods section. In the Results and Discussion section, we present characterizations of nanoparticle colloids, precursor thin films, and CIGS solar absorber layers, and investigate related mechanisms. Finally, we demonstrate CIGS solar cells fabricated directly on Mo sheets with an (active area) conversion efficiency up to 7.37%.

2. EXPERIMENTAL METHODS

Nanoparticle Colloid Synthesis. Figure 1a depicts the LP-PLA setup for synthesis of the metallic nanoparticle colloids. The laser in use is a high-energy femtosecond pulsed laser with 1040 nm wavelength, 600 fs pulse duration, 10 μJ pulse energy, and 500 kHz pulse repetition rate. The laser beam is directed via an automated mirror scanner, and focused through a 170 mm focal lens on the surface of an alloy target submerged at approximately 5 mm beneath a liquid solvent. The solvent is a common organic solvent such as a ketone or an alcohol. The targets in use include Cu−In, Cu−Ga, and Cu−In−Ga alloys with different compositions. Details of target compositions can be found in the Supporting Information. The LP-PLA nanocolloids are stable without adding any stabilizing ligand.

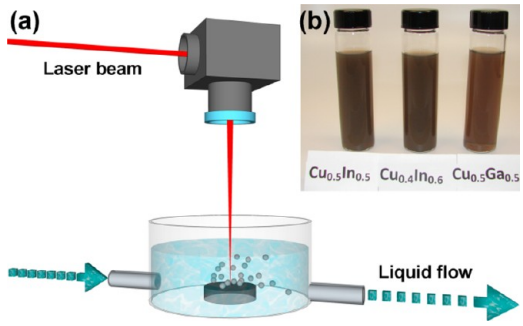

Figure 1. (a) Schematic illustration of generating metallic nanoparticle colloids by LP-PLA. (b) Photo of the as-ablated colloids with different nominal compositions.

Figure 1b shows examples of Cu−In and Cu−Ga alloy colloids fabricated in acetone (Alfa Aesar, 99.5%). Ablation of 15 mins produces 50 ml of colloids with a weight concentration of 0.3 mg/mL. The as-ablated colloid is then used for next thin film deposition without transferring to another solvent.

Precursor Thin-Film Deposition. Figure 2 illustrates a two-electrode EPD vessel where the nanoparticles in the as-ablated colloid

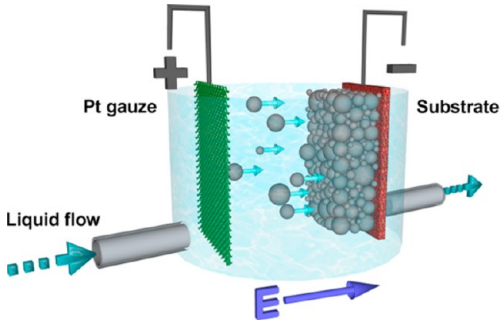

Figure 2. Schematic illustration of cathodic EPD of the nanoparticles in an electrical field.

are deposited on the working electrode (substrate) to form the precursor thin film. An electric field of 100−300 V/cm is applied on the 20 mm×30 mm electrodes at 10 mm apart. The nanoparticle thin film is formed at a deposition rate of 0.5−-5 μm/min, depending on the electric field strength. The working electrode is either a thin Mo sheet (130 μm thick) or a glass substrate coated with a 500 nm thick Mo layer. Before deposition, the substrate is cleaned by sequentially rinsing with acetone, 2.7 M NH_4OH solution, and deionized water. The counter electrode is a Pt gauze. Low concentration (~10 μM) of $In(NO_3)_3$ or $Ga(NO_3)_3$ is added to the colloid before deposition. The purpose of this additive is discussed in the Results and Discussion section. After deposition, the precursor film is quickly transferred through ambient air to a tube furnace for selenization.

Selenization and Device Fabrication. Precursor films are selenized at 500 °C for 15 mins under Se vapor in a tube furnace (5 cm diameter) with atmospheric-pressure Ar flow. The Se vapor is produced by evaporating solid Se pellets placed in the same container (a graphite box) holding the precursor films.

After selenization, the films are subjected to a 2-min etching in 2 wt % KCN aqueous solution to remove possible $Cu_{2-x}Se$ secondary phase, followed by deposition of a 50 nm thick CdS window layer by chemical bath deposition. A 100 nm thick intrinsic ZnO layer and a 300 nm thick ITO layer are deposited by RF sputtering, and a Ni/Au top contact is deposited by DC sputtering. The device is divided into individual test cells (3 mm × 6 mm) by mechanical scribing.

Materials and Device Characterization. The composition, morphology, and microstructure of the nanoparticles are examined using high-resolution transmission electron microscopy (HRTEM),

selected area electron diffraction (SAED), and energy-dispersive spectrometry (EDS). The precursor films and the selenized films are examined using plane-view and cross-sectional scanning electron microscopy (SEM) and X-ray diffraction (XRD). Raman scattering and secondary ion mass spectrometry (SIMS) are used to check phases and impurity concentrations in the films, respectively. Zeta potential of colloidal nanoparticles is measured using dynamic light scattering with a Malvern Zetasizer.

IV characteristics of the solar cells are measured under standard AM1.5G illumination at 1000 W/m^2 intensity using a Newport Oriel IV-station. Calibration of the illumination intensity is performed using a Newport Oriel PV reference cell system coupled with an Oriel/VLSI certified monocrystalline Si reference solar cell. External Quantum Efficiency (EQE) is measured between 300 nm and 1100 nm without light bias using an Oriel QE measurement system equipped with photon flux calibration. Additional experimental details can be found in the Supporting Information.

3. RESULTS AND DISCUSSION

Electrostatic Stabilization of Laser-Ablation-Generated Colloids. The laser-ablation-generated metallic nanoparticles spontaneously form a stable dispersant in the solvent. During the LP-PLA process, the laser beam produces an average energy density of 0.3−1 J/cm^2 at the focal point, and excites a high density plasma plume from the target surface. The plasma is confined and quenched by the ambient solvent, resulting in formation of surface-charged spherical nanoparticles. Without additional stabilizers, the as-formed metallic nanocolloid is stable against aggregation as evidenced by the measured zeta potential (ζ) ranging between −60 and −80 mV for Cu−In and Cu−Ga colloids produced in acetone.

Generally for oxide (MO_x) particles dispersed in aqueous solvents, it is known that pH-controlled dissociation of hydroxyl groups (M−OH) on the oxide surface is responsible for surface charge acquired by the originally neutral oxide particles.[32] In the LP-PLA process, the exact surface charging mechanism of laser-ablated metallic nanoparticles is still under investigation. Previous studies of LP-PLA mainly focus on water as the solvent. It is proposed that partial oxidation of the metal surfaces by the highly reactive laser plasma leads to the charging of even noble metallic nanoparticles such as gold nanoparticles in water.[33,34]

In this work, we observe that in pure organic solvents without stabilizers, given the same ablation parameters, the polarity and magnitude of the surface charge of Cu−In and Cu−Ga nanoparticles are influenced by the solvent ability to donate or accept protons (H^+), namely the solvent proticity. Table 1 compares the measured ζ potential of laser-ablated metallic colloids with respect to the solvatochromic parameters[35] α and β, which quantify the solvent proticity. Here α is the hydrogen-bond donor (HBD) acidity and β is the hydrogen-bond acceptor (HBA) basicity of the solvent. It is observed that positive ζ potential (positive surface charge) is obtained in HBD (protic) solvents with α close to 1 (e.g., methanol), whereas negative ζ potential (negative surface charge) is obtained in HBA (aprotic) solvents with α close to 0 (e.g., acetone). For the two most protic and aprotic solvents (i.e., methanol and acetone, respectively), we suggest that protonation or deprotonation plays an important role in influencing the polarity of the surface charge. Considering the high reactivity in laser-induced plasma and possible surface oxidation due to dissolved oxygen in solvents, it is the preference to absorb or release H^+ (available in protic solvents and lack in aprotic solvents) on the surface oxidation sites that determines the particle surface charge polarity. And the magnitude of ζ potential, which reflects the colloid stability, can be understood by the difference between α and β. The larger the difference is, the more stable the colloid is. This is confirmed in Table 1 that the largest magnitude of ζ potential is measured for colloids produced in acetone, and the relatively smaller ζ values are measured for colloids produced in ethanol and 2-propanol, which are considered HBA-D solvents with both high numbers of α and β.

Table 1. Dependence of Measured ζ Potential of Laser-Ablated Cu, In, Cu−In, and Cu−Ga Colloids on Solvatochromic Parameters α and β[35] of the Solvents

	solvatochromic parameters[35]		measured ζ potential of colloids (mV)			
solvent	α	β	Cu	In	Cu−In	Cu−Ga
methanol	0.93	0.62	33±16	20±10	55±15	23±18
ethanol	0.83	0.77	47±16	2±8	7±11	-8±15
2-propanol	0.76	0.95	11±21	-11±16	29±14	-26±31
acetone	0.08	0.48	-57±18	-36±11	-70±40	-76±48

Surface charging of laser-ablation-generated metallic nanoparticles can be a more complex process than solvent protonation/deprotonation. Considering the highly active metallic nanoparticle surface, reactions between solvent and nanoparticles may also contribute to surface charging. For example, reduction of acetone (by forming an alcohol) can also lead to negative surface charging, and different oxidation level between different nanoparticle materials (e.g., between Cu and In) can account for the different ζ potentials measured in the same solvent. More studies are needed to further clarify the mechanisms.

Nanoparticle Alloy Phases. Regardless of the various targets used for ablation in this work, we find that all nanoparticles have multiple alloy phases and composite structure. The TEM image of Figure 3a shows an example of Cu−In nanoparticles with average size of 70 nm ± 30 nm. The indexed SAED ring pattern (inset of Figure 3a) indicates a dominant polycrystalline Cu_2In phase for the nanoparticle ensemble. Single-crystalline phases are occasionally observed for individual nanoparticles, evidenced by sharp spotty SAED patterns, as shown in Figure 3b, which is recorded from the center of a 100 nm Cu−In nanoparticle and indexed to the hexagonal Cu_2In phase. In addition, we have also observed single-crystalline In phase as previously reported.[36] For Cu−Ga nanoparticles, Cu_9Ga_4 is the dominant phase as suggested by the indexed SAED pattern of Figure 3c. Figure 3d is a HRTEM image revealing composite crystalline structure inside a Cu−Ga nanoparticle and Moire fringes due to lattice overlapping.

Neither SAED nor EDS measurement detects any oxide phase in these alloy nanoparticles produced in ketones and alcohols. This is critical for precise composition control of the final CIGS films, as discussed next.

Nanoparticle Ensemble Composition. Preservation of stoichiometry is a critical issue for employing pulsed laser ablation as a method for complex material synthesis. Stoichiometric loss has been previously observed with long-period and high-power nanosecond laser ablation in vacuum.[37] In this work, we find that the as-ablated metallic nanoparticles, as an ensemble, retain the same atomic composition as that of the original alloy target, with a deviation of no more than ±2 at. %. We attribute such effect to the ultrashort pulse duration of the laser used in ablation. Our previous studies[38] have indicated

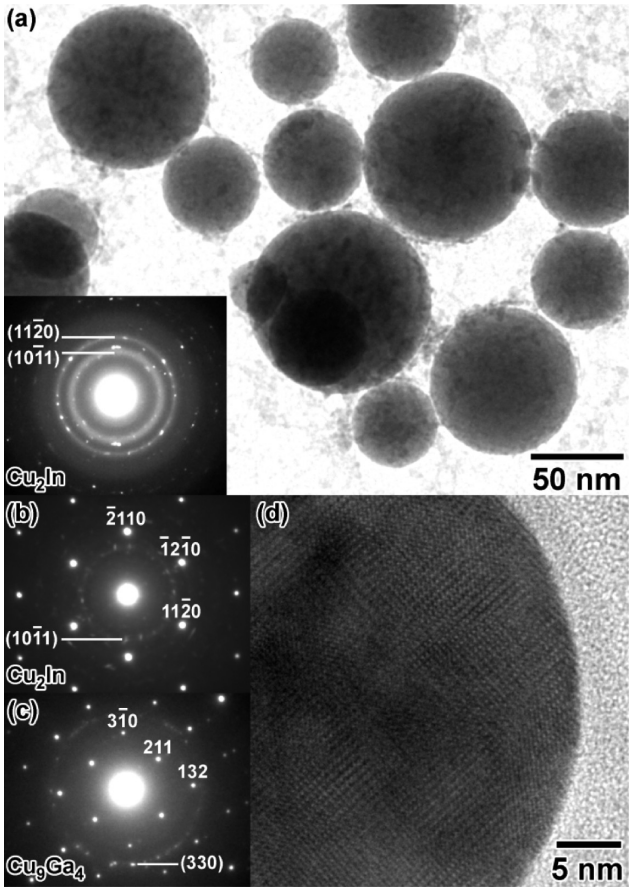

Figure 3. (a) TEM image of an ensemble of Cu−In nanoparticles fabricated in acetone. The inset SAED pattern indicates polycrystalline Cu_2In phase. (b) Indexed SAED pattern of a Cu−In nanoparticle recorded along ⟨0001⟩ zone axis of Cu_2In. (c) Indexed SAED pattern of a Cu−Ga nanoparticle recorded along <$\bar{1}$35> zone axis of Cu_9Ga_4. (d) HRTEM image of a single Cu−Ga nanoparticle.

that at medium to low laser energy density ($<1 \times 10^{12}$ W/cm^2), even individual nanoparticles can retain the original alloy target composition. This phenomenon has later been explained as a result of an ultrafast-laser-induced mechanical fragmentation of the target material.[39]

The overall nanoparticle composition of the colloid is optimized at a desired ratio for CIGS solar cell: approximately Cu/(In + Ga) = 0.85 and Ga/(In + Ga) = 0.3. Such composition control is accomplished by choosing the same target composition of $Cu_{0.46}In_{0.37}Ga_{0.17}$, or alternatively by mixing two colloids, for example $Cu_{0.5}Ga_{0.5}$ and $Cu_{0.4}In_{0.6}$, with a proper volume ratio. Because the nanoparticles contain no detectable oxides as described earlier, the optimized colloid composition should lead to a desired composition in the selenized CIGS film.

Nanoparticle Surface Charge Modulation in EPD. As illustrated in Figure 2, influenced by the electric field during EPD, charged nanoparticles migrate toward the oppositely-charged electrode, becoming neutralized and deposited on the electrode surface. The general kinetics of the EPD process is explained with the Hamaker's law,[40] where variable parameters include the electrical field, conductivity and viscosity of the solvent, and concentration and ζ potential of the nanoparticles. In this work, these parameters are chosen to ensure the following conditions: (1) repulsive forces between nanoparticles are overcome by the electric field at the electrode vicinity so that deposition can occur, and (2) nanoparticles have sufficient time and energy to migrate on the electrode surface before settling down to form a dense-packed film. Particularly noteworthy in this study is that the solvent acetone with low ionic conductivity ($\alpha \rightarrow 0$) is used to provide high EPD rate and uniform coating. This is in agreement with recent results[31] on EPD that the solvent resistivity affects the electric field strength, and thus has an impact on the EPD deposition rate.

To prevent oxidation that can occur on the anode side, cathodic EPD is preferred, i.e., nanoparticles with positive ζ potential are deposited on the negative electrode, rather than vice versa (anodic EPD). To enable cathodic EPD, the negative ζ potential of as-ablated colloid in acetone needs to be reversed to positive. We find that a low concentration of nitrate salts with trivalent cations (M^{3+}) is effective for this purpose. Particularly, In^{3+} or Ga^{3+} is used in this work to minimize the impurities for CIGS. Figure 4 shows that by adding 5 μM and

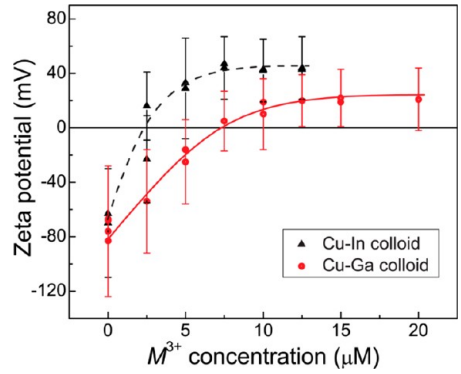

Figure 4. Zeta potential measured for Cu−In and Cu−Ga colloids in acetone with various concentrations of added trivalent cations.

10 μM of trivalent cations to Cu−In and Cu−Ga colloids, respectively, it is adequate to shift their ζ potentials from negative to positive. It can be understood as a result of physical adsorption of the high valence heavy cations on particle surfaces, which has been known to be effective in altering colloidal particle surface charge.[41]

Precursor Films. The EPD deposited alloy films typically have a metallic dark grey color. Without using binders in deposition, close-packed and crack-free films are deposited as shown in SEM images a and b in Figure 5. (Smoother films can be obtained with polymer binders however without improving overall CIGS quality after seleinzation.) XRD measurements of the Cu−In and Cu−Ga films (Figure 5c) confirm the same crystalline phases of Cu_2In, In, and Cu_9Ga_4 as those identified using TEM SAED analysis. Note that the Mo metal sheet manufactured by a rolling process has a different out-of-plane orientation of [211] at $2\theta = 73.7°$, in comparison to that of [110] at $2\theta = 40.5°$ for a thin Mo layer coated on glass.

CIGS Films. Images a and b in Figure 6 show the CIGS films formed on Mo-coated glass substrates after selenization. The films have smooth surfaces and large micrometer-size grains. However, a thick $MoSe_2$ interfacial layer and some voids at the CIGS/$MoSe_2$ interface are observed. Solar cells with better device performance are accomplished on Mo metal sheet substrates. The corresponding CIGS film surface and device cross-section are shown in images c and d in Figure 6, respectively. Although the grains are smaller compared with the

dx.doi.org/10.1021/am3022976 | ACS Appl. Mater. Interfaces 2012, 4, 7036−7042

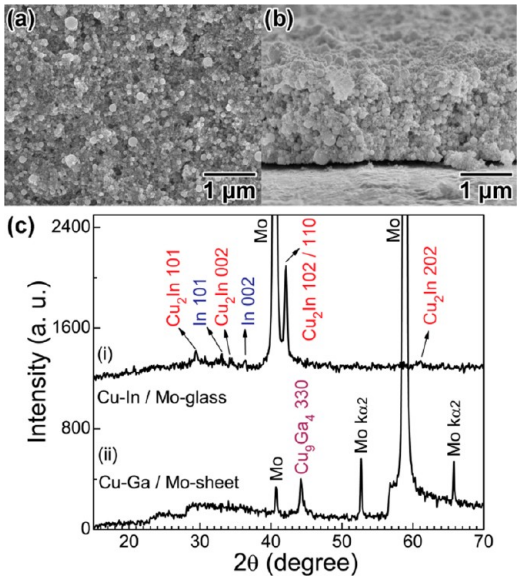

Figure 5. (a) Plane-view and (b) cross-sectional SEM images of as-deposited precursor films on Mo metal sheets. (c) XRD patterns of as-deposited (i) Cu–In and (ii) Cu–Ga alloy films on Mo-coated glass and Mo metal sheet substrates, respectively. The small gap between film and substrate in (b) is formed when bending the sample for cross-sectional imaging.

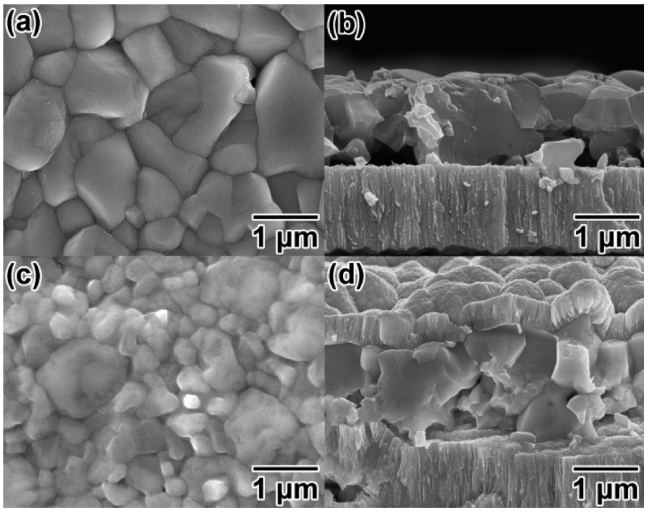

Figure 6. Plane-view and cross-sectional SEM images of selenized CIGS films on (a, b) Mo-coated glass and (c, d) Mo metal sheet. The film in (d) is coated with CdS, ZnO, and ITO layers on top.

films obtained on Mo-coated glass substrates, the CIGS films on Mo metal sheets have fewer voids at the CIGS/$MoSe_2$ interface. The CIGS films on Mo sheets have a Cu-poor composition of approximately Cu/(In+Ga) = 0.88 where Ga/(In+Ga) = 0.21, as analyzed from plane-view SEM-EDS measurements where electron beam (20 keV) incidents normally on the film surface. The deviation of the final film composition from that of the original colloid is probably due to segregation of Ga (Figure S1 in the Supporting Information) to the film bottom, which is an issue currently under optimization.

The selenized CIGS films are checked for impurity phases using XRD and Raman scattering. Figure 7a shows a typical XRD pattern of the CIGS films grown on Mo sheets, indicating polycrystalline CIGS structure with a predominant [112] out-

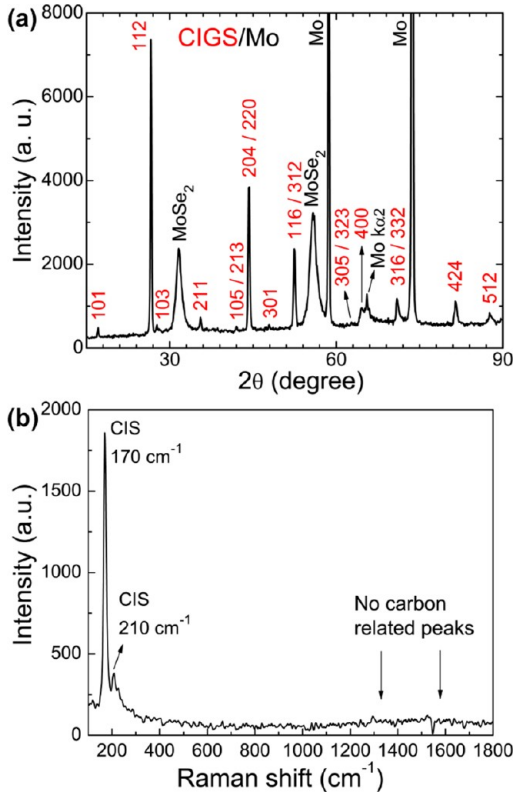

Figure 7. (a) XRD pattern and (b) Raman spectrum measured from the CIGS film on Mo metal sheet substrate.

of-plane orientation. Except $MoSe_2$-related peaks, no other secondary and impurity phases such as $Cu_{2-x}Se$ and In_2O_3 are detected. Figure 7b shows that the Raman spectrum is dominated by two CIS phonon modes[42] at 170 and 210 cm^{-1}, without significant carbon-related modes typically appearing between 1300 and 1600 cm^{-1}.[43] SIMS measurement confirms the film purity by revealing a low atomic concentration of 2–5 × 10^{18} cm^{-3} for carbon impurity in the selenized CIGS films, which is close to the instrument detection limit in CIGS material.

CIGS Solar Cells. To improve statistics, we scribe the samples into small cells of approximately 3 mm × 6 mm^2 size as shown in Figure 8a inset. Current–voltage (I–V) characteristics of finished solar cells without anti-reflection coating exhibit total area (0.170 cm^{-2}) efficiencies varying in the range of 3.9-5.8%, and averaging at 5.0%. Figure 8a also shows the stabilized I–V characteristic of a CIGS cell on Mo sheet, with an active area (0.132 cm^{-2}) efficiency of 7.37% after subtracting the Ni/Au contact area (about 22% of the total cell size). Other cell parameters include: an open-circuit voltage (V_{OC}) of 0.363 V, a short-circuit current density (J_{SC}) of 34.58 mA/cm^2, a fill factor (FF) of 58.76%, a series resistance (R_S) of 2.75 Ω cm^2, and a shunting resistance (R_{Sh}) of 216 Ω cm^2.

The V_{OC} is lower than those values reported for high-efficient vacuum-deposited CIGS solar cells. This can be caused by a few factors, including (1) localized shunting pinholes correlating with the low R_{Sh} value and originating from the rough surface of the Mo metal sheet, and (2) segregation of Ga to film bottom, which reduces the bandgap at the top of the absorber layer. We have observed that films grown on smooth Mo-coated glass substrates display a much smoother surface morphology and larger grains (Figure 6a). Reducing of pinholes on the films

dx.doi.org/10.1021/am3022976 | ACS Appl. Mater. Interfaces 2012, 4, 7036–7042

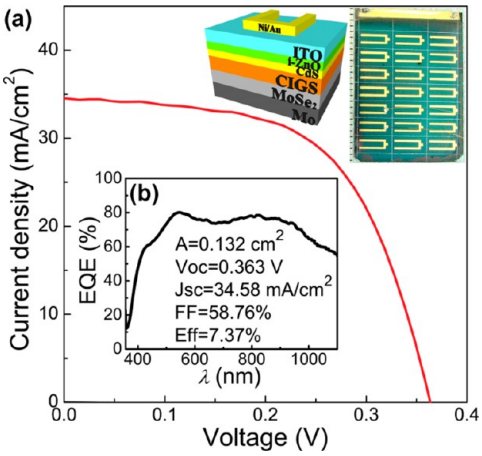

Figure 8. (a) *I*–*V* and (b) EQE characteristics measured for the CIGS solar cell on Mo metal sheet as shown in Figure 6d. The inset photo and illustration show the solar cell and its device structure, respectively.

grown on Mo sheets can be expected when a smoother Mo sheet surface is available. Using cross-sectional SEM-EDS (see Figure S1 in the Supporting Information), we have also observed a higher Ga content near the film-substrate interface than at the top half of the films. The relatively low FF is mostly due to a thick $MoSe_2$ layer (1–1.5 μm) formed during selenization that significantly increases R_S. We expect further improvement of efficiency after minimizing the Mo substrate selenization.

Figure 8b shows that the external quantum efficiency (EQE) measured without light bias on this device is about 70-80% between 500 and 1000 nm. The slight drop of EQE between 550 and 800 nm indicates recombination loss caused by structural defects in the CIGS layer.

4. CONCLUSIONS

In summary, LP-PLA is applied in ligand-free synthesis of metallic nanoparticles with preserved alloy composition and negligible oxidation in common organic solvents. The nanoparticle surface charge is influenced by the solvent proticity, and can be modulated with low concentration of trivalent metal cations without affecting the colloid purity. The surface charge modulated nanoparticles are suitable for thin film deposition by EPD without solvent transfer and without using binders. On the basis of these studies, we have established an expedient way of fabricating metallic nanoparticle thin films with high purity and precise composition. After selenization, high quality CIGS films are obtained and 7.37%-efficient (active area) CIGS solar cells are fabricated directly on Mo metal sheets. This approach for fabricating thin film solar cells has minimized chemical impurities, fast deposition rate, high raw material utilization, and is also applicable to other materials such as CZTS.

■ ASSOCIATED CONTENT

Supporting Information

Additional experimental details and analysis. This material is available free of charge via the Internet at http://pubs.acs.org.

■ AUTHOR INFORMATION

Corresponding Author

*Tel: 1-734-930-2583. Fax: 1-734-669-7403. E-mails: wguo@imra.com.

Notes

The authors declare no competing financial interest.

■ ACKNOWLEDGMENTS

The authors thank Dr. Kai Sun from the Department of Materials Science and Engineering at the University of Michigan–Ann Arbor for his help in TEM experiments and discussions.

■ REFERENCES

(1) Coutts, T. J.; Osterwald, C. R. *Sol. Cells* **1987**, *22*, 195–209.
(2) Jackson, P.; Hariskos, D.; Lotter, E.; Paetel, S.; Wuerz, R.; Menner, R.; Wischmann, W.; Powalla, M. *Prog. Photovolt.: Res. Appl.* **2011**, *19*, 894–897.
(3) Repins, I.; Contreras, M. A.; Egaas, B.; DeHart, C.; Scharf, J.; Perkins, C. L.; To, B.; Noufi, R. *Prog. Photovolt.: Res. Appl.* **2008**, *16*, 235–239.
(4) Todorov, T. K.; Gunawan, O.; Gokmen, T.; Mitzi, D. B. *Prog. Photovolt.: Res. Appl.* **2012**, DOI: 10.1002/pip.1253.
(5) Todorov, T. K.; Tang, J.; Bag, S.; Gunawan, O.; Gokmen, T.; Zhu, Y.; Mitzi, D. B. *Adv. Energy Mater.* **2012**, DOI: 10.1002/aenm.201200348..
(6) Lincot, D.; Guillemoles, J. F.; Taunier, S.; Guimard, D.; Sicx-Kurdi, J.; Chaumont, A.; Roussel, O.; Ramdani, O.; Hubert, C.; Fauvarque, J. P.; Bodereau, N.; Parissi, L.; Panheleux, P.; Fanouillere, P.; Naghavi, N.; Grand, P. P.; Benfarah, M.; Mogensen, P.; Kerrec, O. *Sol. Energy* **2004**, *77*, 725–737.
(7) Calixto, M. E.; Dobson, K. D.; McCandless, B. E.; Birkmire, R. W. *J. Electrochem. Soc.* **2006**, *153*, G521–G528.
(8) Aksu, S.; Lastella, S.; Kleiman-Shwarsctein, A.; Pinarbasi, M. *ECS Trans.* **2011**, *35*, 33–38.
(9) Bhattacharya, R. N.; Oh, M. K.; Kim, Y. *Sol. Energy Mater. Sol. Cells* **2012**, *98*, 198–202.
(10) Kaelin, M.; Rudmann, D.; Kurdesau, F.; Zogg, H.; Meyer, T.; Tiwari, A. N. *Thin Solid Films* **2005**, *480*, 486–490.
(11) Wang, W.; Su, Y. W.; Chang, C. H. *Sol. Energy Mater. Sol. Cells* **2011**, *95*, 2616–2620.
(12) Uhl, A. R.; Romanyuk, Y. E.; Tiwari, A. N. *Thin Solid Films* **2011**, *519*, 7259–7263.
(13) Wang, W.; Han, S.-Y.; Sung, S.-J.; Kim, D.-H.; Chang, C.-H. *Phys. Chem. Chem. Phys.* **2012**, *14*, 11154–11159.
(14) Ahn, S.; Kim, K. H.; Yun, J. H.; Yoon, K. H. *J. Appl. Phys.* **2009**, *105*, 113533.
(15) Schulz, D. L.; Curtis, C. J.; Flitton, R. A.; Wiesner, H.; Keane, J.; Matson, R. J.; Jones, K. M.; Parilla, P. A.; Noufi, R.; Ginley, D. S. *J. Electron. Mater.* **1998**, *27*, 433–437.
(16) Ahn, S.; Kim, K.; Cho, A.; Gwak, J.; Yun, J. H.; Shin, K.; Ahn, S.; Yoon, K. *ACS Appl. Mater. Interfaces* **2012**, *4*, 1530–1536.
(17) Akhavan, V. A.; Goodfellow, B. W.; Panthani, M. G.; Reid, D. K.; Hellebusch, D. J.; Adachi, T.; Korgel, B. A. *Energy Environ. Sci.* **2010**, *3*, 1600–1606.
(18) Guo, Q.; Ford, G. M.; Yang, W. C.; Walker, B. C.; Stach, E. A.; Hillhouse, H. W.; Agrawal, R. *J. Am. Chem. Soc.* **2010**, *132*, 17384–17386.
(19) Panthani, M. G.; Akhavan, V.; Goodfellow, B.; Schmidtke, J. P.; Dunn, L.; Dodabalapur, A.; Barbara, P. F.; Korgel, B. A. *J. Am. Chem. Soc.* **2008**, *130*, 16770–16777.
(20) Guo, Q.; Ford, G. M.; Agrawal, R.; Hillhouse, H. W. *Prog. Photovolt.: Res. Appl.* **2012**, DOI: 10.1002/pip.2200.
(21) Kapur, V. K.; Bansal, A.; Le, P.; Asensio, O. I. *Thin Solid Films* **2003**, *431*, 53–57.
(22) Norsworthy, G.; Leidholm, C. R.; Halani, A.; Kapur, V. K.; Roe, R.; Basol, B. M.; Matson, R. *Sol. Energy Mater. Sol. Cells* **2000**, *60*, 127–134.
(23) Kaelin, M.; Rudmann, D.; Kurdesau, F.; Meyer, T.; Zogg, H.; Tiwari, A. N. *Thin Solid Films* **2003**, *431*, 58–62.
(24) Chen, G. B.; Wang, L.; Sheng, X.; Yang, D. R. *J. Mater. Sci.–Mater. Electron.* **2011**, *22*, 1124–1129.

(25) Talapin, D. V.; Lee, J. S.; Kovalenko, M. V.; Shevchenko, E. V. *Chem. Rev.* **2010**, *110*, 389−458.
(26) Zhang, F.; Lees, E.; Amin, F.; Gil, P. R.; Yang, F.; Mulvaney, P.; Parak, W. J. *Small* **2011**, *7*, 3113−3127.
(27) Nag, A.; Kovalenko, M. V.; Lee, J. S.; Liu, W. Y.; Spokoyny, B.; Talapin, D. V. *J. Am. Chem. Soc.* **2011**, *133*, 10612−10620.
(28) Barsch, N.; Jakobi, J.; Weiler, S.; Barcikowski, S. *Nanotechnology* **2009**, *20*, 445603.
(29) Amendola, V.; Meneghetti, M. *Phys. Chem. Chem. Phys.* **2009**, *11*, 3805−3821.
(30) Besra, L.; Liu, M. *Prog. Mater. Sci.* **2007**, *52*, 1−61.
(31) Dickerson, J. H.; Boccaccini, A. R., In *Electrophoretic Deposition of Nanomaterials*; Springer: New York, 2012; p 119.
(32) Boch, P.; Niepce, J. C., In *Ceramic Materials Processes, Properties and Applications*; ISTE: London, 2007; p 133134.
(33) Sylvestre, J. P.; Poulin, S.; Kabashin, A. V.; Sacher, E.; Meunier, M.; Luong, J. H. T. *J. Phys. Chem. B* **2004**, *108*, 16864−16869.
(34) Muto, H.; Yamada, K.; Miyajima, K.; Mafune, F. *J. Phys. Chem. C* **2007**, *111*, 17221−17226.
(35) Kamlet, M. J.; Abboud, J. L. M.; Abraham, M. H.; Taft, R. W. *J. Org. Chem.* **1983**, *48*, 2877−2887.
(36) Guo, W.; Hagedorn, K.; Liu, B. *Proc. SPIE* **2011**, *8104*, 81040W DOI: 10.1117/12.894109.
(37) Young, K. H. *Physica C* **1993**, *211*, 1−12.
(38) Liu, B.; Hu, Z. D.; Che, Y. *Laser Focus World* **2007**, *43*, 74−76.
(39) Itina, T. E. *Appl. Surf. Sci.* **2009**, *255*, 5107−5111.
(40) Hamaker, H. C. *Trans. Faraday Soc.* **1940**, *35*, 0279−0286.
(41) Hiemenz, P. C.; Rajagopalan, R., In *Principles of Colloid and Surface Chemistry*, 3rd ed.; Marcel Dekker: New York, 1997; p 588.
(42) Tanino, H.; Maeda, T.; Fujikake, H.; Nakanishi, H.; Endo, S.; Irie, T. *Phys. Rev. B* **1992**, *45*, 13323−13330.
(43) Tuinstra, F.; Koenig, J. L. *J. Chem. Phys.* **1970**, *53*, 1126.